Thermal analysis of line-defect photonic crystal lasers

Xue, Weiqi; Ottaviano, Luisa; Chen, Yaohui; Semenova, Elizaveta; Yu, Yi; Lupi, Alexandra; Mørk, Jesper; Yvind, Kresten

Published in:
Optics Express

Link to article, DOI:
10.1364/OE.23.018277

Publication date:
2015

Document Version
Publisher's PDF, also known as Version of record

Thermal analysis of line-defect photonic crystal lasers

Weiqi Xue,[1,*] Luisa Ottaviano,[1] Yaohui Chen, Elizaveta Semenova, Yi Yu, Alexandra Lupi, Jesper Mork, and Kresten Yvind

DTU Fotonik, Department of Photonics Engineering, Technical University of Denmark, Build. 343, DK-2800 Kongens Lyngby, Denmark

[1]These authors contributed equally to this work.

[*]wexu@fotonik.dtu.dk

Abstract: We report a systematic study of thermal effects in photonic crystal membrane lasers based on line-defect cavities. Two material platforms, InGaAsP and InP, are investigated experimentally and numerically. Lasers with quantum dot layers embedded in an InP membrane exhibit lasing at room temperature under CW optical pumping, whereas InGaAsP membranes only lase under pulsed conditions. By varying the duty cycle of the pump beam, we quantify the heating induced by optical pumping in the two material platforms and compare their thermal properties. Full 3D finite element simulations show the spatial temperature profile and are in good agreement with the experimental results concerning the thermal tolerance of the two platforms.

OCIS codes: (230.5298) Photonic crystals; (140.3460) Lasers.

References and links

1. J. D. Joannopoulos, P. R. Villeneuve, and S. Fan, "Photonic crystals: putting a new twist on light," Nature **386**(6621), 143–149 (1997).
2. Y. Akahane, T. Asano, B. S. Song, and S. Noda, "High-Q photonic nanocavity in a two-dimensional photonic crystal," Nature **425**(6961), 944–947 (2003).
3. Y. A. Vlasov, M. O'Boyle, H. F. Hamann, and S. J. McNab, "Active control of slow light on a chip with photonic crystal waveguides," Nature **438**(7064), 65–69 (2005).
4. H. Sekoguchi, Y. Takahashi, T. Asano, and S. Noda, "Photonic crystal nanocavity with a Q-factor of ~9 million," Opt. Express **22**(1), 916–924 (2014).
5. Y. Lai, S. Pirotta, G. Urbinati, D. Gerace, M. Minkov, V. Savona, A. Badolato, and M. Galli, "Genetically designed L3 photonic crystal nanocavities with measured quality factor exceeding one million," Appl. Phys. Lett. **104**(24), 241101 (2014).
6. J. Li, T. P. White, L. O'Faolain, A. Gomez-Iglesias, and T. F. Krauss, "Systematic design of flat band slow light in photonic crystal waveguides," Opt. Express **16**(9), 6227–6232 (2008).
7. L. H. Frandsen, A. V. Lavrinenko, J. Fage-Pedersen, and P. I. Borel, "Photonic crystal waveguides with semi-slow light and tailored dispersion properties," Opt. Express **14**(20), 9444–9450 (2006).
8. B. Corcoran, C. Monat, C. Grillet, D. J. Moss, B. J. Eggleton, T. P. White, L. O'Faolain, and T. F. Krauss, "Green light emission in silicon through slow-light enhanced thire-harmonic generation in photonic-crystal waveguides," Nat. Photonics **3**(4), 206–210 (2009).
9. S. Ek, P. Lunnemann, Y. Chen, E. Semenova, K. Yvind, and J. Mork, "Slow-light-enhanced gain in active photonic crystal waveguides," Nat. Commun. **5**, 5039 (2014).
10. M. Okano, T. Yamada, J. Sugisaka, N. Yamamoto, M. Itoh, T. Sugaya, K. Komori, and M. Mori, "Analysis of two-dimensional photonic crystal L-type cavities with low-refractive-index material cladding," J. Opt. **12**(7), 075101 (2010).
11. K. Inoue, M. Sasada, J. Kawamata, K. Sakoda, and J. Haus, "A two-dimentional photonic crystal laser," Jpn. J. Appl. Phys. **38**(2), L157 (1999).
12. H.-G. Park, J. K. Hwang, J. Huh, H.-Y. Ryu, S.-H. Kim, J.-S. Kim, and Y.-H. Lee, "Characteristics of modified single-defect two-dimensional photonic crystal lasers," IEEE J. Quantum Electron. **38**(10), 1353–1365 (2002).
13. M. Lončar, T. Yoshie, A. Scherer, P. Gogna, and Y. Qiu, "Low-threshold photonic crystal laser," Appl. Phys. Lett. **81**(15), 2680–2682 (2002).
14. M. H. Shih, W. Kuang, A. Mock, M. Bagheri, E. H. Hwang, J. D. O'Brien, and P. D. Dapkus, "High-quality-factor photonic crystal heterostructure laser," Appl. Phys. Lett. **89**(10), 101104 (2006).

#240193 Received 1 May 2015; revised 22 Jun 2015; accepted 29 Jun 2015; published 6 Jul 2015

15. S. Matsuo, T. Sato, K. Takeda, A. Shinya, K. Nozaki, H. Taniyama, M. Notomi, K. Hasebe, and T. Kakitsuka, "Ultralow operating energy electrically driven photonic crystal lasers," IEEE J. Sel. Top. Quantum Electron. **19**(4), 4900311 (2013).
16. M. Nomura, S. Iwamoto, K. Watanabe, N. Kumagai, Y. Nakata, S. Ishida, and Y. Arakawa, "Room temperature continuous-wave lasing in photonic crystal nanocavity," Opt. Express **14**(13), 6308–6315 (2006).
17. L. Lu, A. Mock, M. Bagheri, J.-R. Cao, S.-J. Choi, J. O'Brien, and P. Dapkus, "Gain compression and thermal analysis of a sapphire-bonded photonic crystal microcavity laser," IEEE Photonics Technol. Lett. **21**(17), 1166–1168 (2009).
18. S. Matsuo, A. Shinya, T. Kakitsuka, K. Nozaki, T. Segawa, T. Sato, Y. Kawaguchi, and M. Notomi, "High-speed ultracompact buried heterostructure photonic-crystal laser with 13 fJ of energy consumed per bit transmitted," Nat. Photonics **4**(9), 648–654 (2010).
19. E. S. Semenova, I. V. Kulkova, S. Kadkhodazadeh, M. Schubert, and K. Yvind, "Metal organic vapor-phase epitaxy of InAs/InGaAsP quantum dots for laser applications at 1.5μm," Appl. Phys. Lett. **99**(10), 101106 (2011).
20. M. Schubert, T. Suhr, S. Ek, E. S. Semenova, J. M. Hvam, and K. Yvind, "Lambda shifted photonic crystal cavity lasers," Appl. Phys. Lett. **97**(19), 191109 (2010).
21. S. Adachi and H. Kawaguchi, "Chemical etching characteristics of (001) InP," J. Electrochem. Soc. **128**(6), 1342–1349 (1981).
22. D. I. Elder and A. R. Clawson, "Determination of $In_{0.53}Ga_{0.47}As$ layer thicknesses from etched step," J. Mater. Sci. Lett. **3**(4), 340 (1984).
23. L. A. Coldren and S. W. Corzine, *Diode Lasers and Photonic Integrated Circuits* (John Wiley & Sons, 1995).
24. M. Asada and Y. Suematsu, "The effects of loss and nonradiative recombination on the temperature dependence of threshold current in 1.5–1.6 μm GaInAsP/InP lasers," IEEE J. Quantum Electron. **19**(6), 917–923 (1983).
25. Y. Zou, J. S. Osinski, P. Grodzinski, P. D. Dapkus, W. C. Rideout, W. F. Sharfin, J. Schlafer, and F. D. Crawford, "Experimental study of auger recombination, gain, and temperature sensitivity of 1.5 μm compressively strained semiconductor lasers," IEEE J. Quantum Electron. **29**(6), 1565–1575 (1993).
26. M. N. Sysak, H. Park, A. W. Fang, J. E. Bowers, R. Jones, O. Cohen, O. Raday, and M. J. Paniccia, "Experimental and theoretical thermal analysis of a Hybrid Silicon Evanescent Laser," Opt. Express **15**(23), 15041–15046 (2007).
27. B. Mroziewicz, M. Bugajski, and W. Nakwaski, *Physics of Semiconductor Lasers* (Elsevier, 1991).
28. M. Bertolotti, V. Bogdanov, A. Ferrari, A. Jascow, N. Nazorova, A. Pikhtin, and L. Schirone, "Temperature dependence of the refractive index in semiconductors," J. Opt. Soc. Am. B **7**(6), 918–922 (1990).

1. Introduction

Photonic Crystal (PhC) membrane structures offer exciting possibilities for controlling light propagation and light-matter interactions in ultra-small structures and have attracted extensive attention the past decades [1]. Point-defects in the periodic pattern of air-holes in the membrane can be used to realize high-quality nano-cavities [2] and line-defects allow the realization of waveguides, which feature slow light propagation [3]. Many impressive achievements have already been reported, including measured quality (Q) factors exceeding a few million [4, 5], flat-band slow light by dispersion engineering [6, 7], enhanced nonlinearities [8] and slow-light enhanced gain [9]. By omitting only a finite number (N) of air-holes in a line, a so-called LN-cavity can be realized [10]. Compared to conventional Fabry-Perot or DFB edge-emitting lasers, such micro cavity lasers have many interesting characteristics, such as ultra-small size, with the possibility of close-to-diffraction-limited mode volume, ultra-low threshold, and on-chip integration [11–15]. However, because the semiconductor membrane has a thickness of a few hundred nanometers and normally is suspended in air, heat generated through the pumping process, either optical or electrical, may accumulate in the structure, making it difficult to achieve continuous-wave (CW) lasing at room temperature [11–14]. Even with the achievement of CW lasing, the laser output power saturates when the pump power is only a few times larger than the laser threshold level [16]. Several approaches have been successfully implemented to overcome the heating accumulation. In [17], a thermally conductive cladding was introduced by bonding the membrane to sapphire, but such approaches also lower the vertical refractive index contrast. In [18], a major development in PhC laser technology was demonstrated by confining a buried-heterostructure active region within the line-defect cavity. Notably, the active region was embedded in an InP membrane, which has much better thermal conductivity than the quaternary material InGaAsP, which was conventionally used [12–14]. Even though thermal

#240193 Received 1 May 2015; revised 22 Jun 2015; accepted 29 Jun 2015; published 6 Jul 2015

effects have long been recognized as a main limiting factor for improving the performance of PhC membrane lasers, a quantitative and comprehensive study of thermal effects in such membrane lasers is, to the best of our knowledge, still missing.

In this work, we present systematic investigations of the thermal properties of InGaAsP and InP photonic crystal membrane lasers. In both cases, the active layers are composed of InAs quantum dots (QDs) and we explain in detail how the structures are fabricated. The properties of lasers based on the two platforms are then experimentally characterized and the pump-induced temperature changes are quantified. Thermal simulations using three-dimensional finite element techniques show good agreement with the experimental observations and reveal the spatial temperature profile in the lasers.

2. Sample fabrication

All our InP membrane samples have been grown in a low-pressure metal organic vapor-phase epitaxy reactor (Discovery 125) on InP (001) substrates using hydrogen as carrier gas at 610°C. The structure contains three layers of QDs separated by 30 nm thick InP layers in the middle of a 250 nm thick InP membrane, formed on top of a 250 nm thick $In_{0.53}Ga_{0.47}As$ etch stop layer. To form an array of QDs the growth temperature was reduced to 485°C during a 2 minutes growth interruption and the layer of InAs with effective thickness of 1.65ML followed 10 nm of InP was deposited. Figure 1(a) shows a High Resolution Scanning Transmission Electron Microscopy (HR STEM) image of the QDs. Alternatively, the epitaxial structure for the InGaAsP membrane based lasers were formed by depositing a 340 nm thick InGaAsP (λ_g = 1.15 μm) layer on top of 1 μm sacrificial layers formed by a stack of 100 nm InP, 100 nm $In_{0.52}Al_{0.48}As$ and 800 nm InP. Details about the growth and the results of the optical and morphological investigation of the QDs used in these membranes can be found in [19]. A detailed description of the fabrication of InGaAsP membrane based devices can be found in [9, 20]. Here we will only focus on the processes for fabricating optically pumped PhC lasers on an air-suspended InP membrane on silicon.

Once the epilayer structure has been grown it is bonded to a Si carrier. In principle, direct III-V/SiO_2/Si bonding could be employed for the fabrication of the hybrid devices, but in the fabrication process we present here we have used Bisbenzocyclobutene (BCB) adhesive bonding. Before that a ~1 μm silicon dioxide (SiO_2) layer is deposited on both the Si and the InP surface by plasma enhanced chemical vapor deposition (PECVD) for a better adhesion of the semiconductor surface to the BCB layer and to allow selective wet etching to obtain an air-suspended membrane. The bonding process is carried out in an EVG bonder, where BCB is cured for 1h at 250 °C in a nitrogen atmosphere, under a piston force of 750 N. After bonding, it is important to remove the BCB covering the sample edges before the substrate removal. This is done in a CF_4/O_2 plasma ashing step and it will prevent the formation of InP cliffs at the edge of the wafer during the following wet etch. The InP substrate and the InGaAs sacrificial layer are selectively wet etched in HCl [21] and H_2SO_4:H_2O_2 [22] solutions, respectively, leaving a very smooth InP membrane bonded to the Si carrier, as shown in Figs. 1(b) and 1(c).

A JEOL JBX-9500 electron beam lithography writer, operating at 100 kV is used to write the PhCs pattern on a high-resolution positive e-beam resist, Zeon's Chemicals ZEP-520A layer. Before spin coating the sample with around 500 nm thick resist layer, A ~200 nm thick SiNx layer has been deposited using PECVD to function as a hard mask. After the exposure, the resist is developed in ZED N50 and then the mask is transferred to the nitride layer in a reactive ion etching (RIE) tool, using a CHF_3/O_2 (15:1sccm) gas chemistry. The nitride etching recipe has been optimized in order to achieve etched sidewalls as smooth and vertical in slope as possible; the SiNx layer thickness has been chosen considering that the etching selectivity to ZEP-520A is ~1:1. At this point the resist layer can be removed in a heated ultrasonic bath of microposit® remover 1165. The use of the SiNx hard mask is necessary because the InP dry etching process is performed in cyclic $CH_4/H_2 – O_2$ gas chemistries that

#240193 Received 1 May 2015; revised 22 Jun 2015; accepted 29 Jun 2015; published 6 Jul 2015

do not perform well with resist masks. Finally the sample is immersed in a BHF solution with a wetting agent to obtain an air suspended membrane and, at the same time, to remove the hard mask. Figure 1(d) shows a SEM image of a fabricated InP L20 cavity. Three QDs layers can be identified from the cross-section of the fabricated PhC membrane, as highlighted by the red lines in Fig. 1(e).

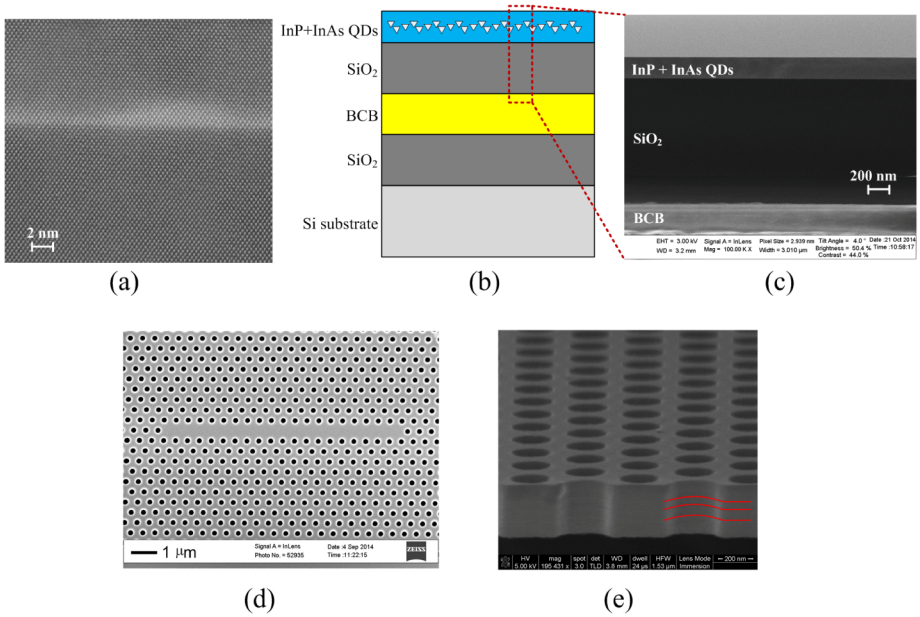

Fig. 1. (a) Cross-sectional HR STEM images of a single QD in InP. (b) Schematic representation of the InP membrane bonded to a Si wafer. (c) Cross section view (made by SEM) of the InP membrane after bonding and substrate removal. (d) SEM image of an InP-membrane laser with an L20 PhC defect cavity. (e) SEM image showing the cross-section of the PhC membrane with three layers of QDs, highlighted by the red lines.

The design parameters for the PhC structures investigated are summarized in Table 1. The InGaAsP samples are of the same structure as reported in [9].The cavity length and Q-factor are thus not exactly same as for the new InP samples. However, these minor differences are thermally in favor of the InGaAsP device and will not affect the conclusions reported here.

Table 1. Main structural parameters for InGaAsP and InP PhC line-defect lasers.

Parameters	*InGaAsP*	*InP*
Lattice constant	380 nm	438 nm
Thickness	340 nm	250 nm
Air-hole radius	85 nm	110 nm
Cavity length	L27/~10.6 µm	L20/~9.2 µm
Calculated passive cavity quality factor	5.2×10^5	1.6×10^5

3. Experimental results

The characterization set-up is shown in Fig. 2. A pulsed pump diode at a wavelength of 980 nm is used to excite the PhC laser samples. The pump pulse width is fixed at 500 ns. The duty cycle (t / T) of the pulse train is variable from 0.1% to 5%. After passing through an optical tunable attenuator, the pump beam is focused on the sample through a microscope objective

#240193 Received 1 May 2015; revised 22 Jun 2015; accepted 29 Jun 2015; published 6 Jul 2015

with a numerical aperture (NA) of 0.65. The spatial profile of the pump beam is monitored using an infrared (IR) camera. For all the measurements presented in this paper, the FWHM - diameter of the pump is fixed at ~10 μm. The emission from the PhC sample is collected vertically using the same objective. After being isolated from the reflected pump beam by a longpass filter, the signal is analyzed using a highly sensitive spectrometer with a cooled array of low-noise InGaAs photodetectors.

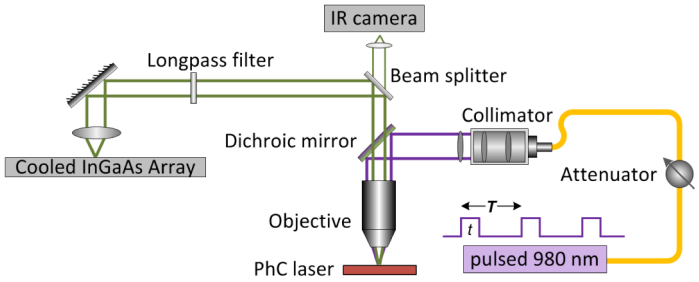

Fig. 2. Characterization set-up. The cooled InGaAs array spectrometer is operating at $-100°c$.

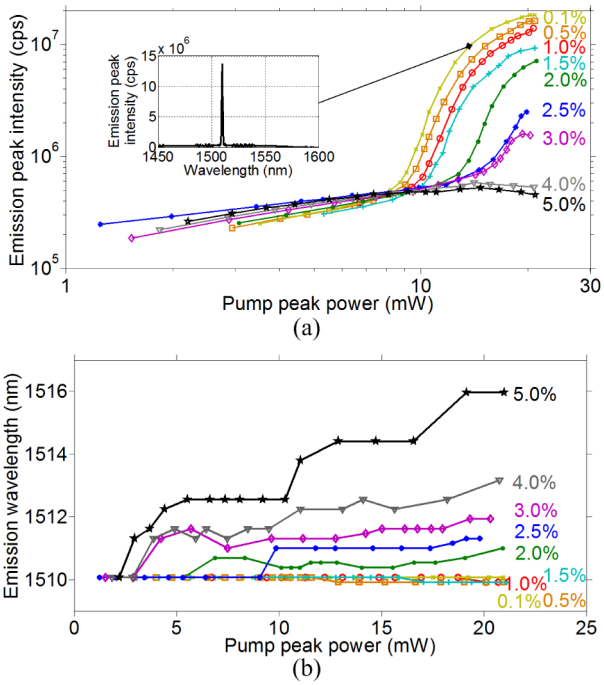

Fig. 3. Measured (a) peak power and (b) wavelength of the emitted pulses from the InGaAsP PhC sample as a function of the peak pump power for various duty cycles of the pump pulse train. The inset in (a) shows the lasing spectrum above threshold for a duty cycle of 0.1% and peak pump power of 14 mW.

We first characterize the InGaAsP sample. For a given duty cycle of the pump pulse train, the measured peak intensity of the pulses emitted from the sample is plotted in Fig. 3(a) as a function of the peak power of the excitation pulse. For duty cycles below 3.0%, a transition to lasing is clearly observed. The inset shows a typical lasing spectrum at a duty cycle of 0.1%. As the duty cycle increases, not only is a larger pump power required in order to reach the lasing threshold, but also the absolute emission power at a given pump level drops

#240193 Received 1 May 2015; revised 22 Jun 2015; accepted 29 Jun 2015; published 6 Jul 2015

significantly. For duty cycles of 4.0% and 5.0%, lasing was not achieved. The corresponding laser wavelength as a function of pump peak power is plotted in Fig. 3(b). The red-shift of the laser wavelength reflects an increase of the refractive index of the membrane due to heating. For duty cycles larger than 1.5%, the laser wavelength shifts significantly with pump power. The abrupt shifts of the measured emission wavelength in Fig. 3(b), especially at the duty cycle of 5.0%, are due to a low signal-to-noise ratio (SNR), since the emitted power is close to the background noise floor.

In general, the membrane is heated since the energy of the pump photons is larger than the energy of the emitted photons. For a pulsed pump with a certain duty cycle, the sample is heated during the 'on-time', and cools down during the 'off-time'. When the duty cycle is smaller than 1.5%, the 'off-time' is long enough for the sample to dissipate most of the generated heat, reaching a steady-state close to room temperature. As the duty cycle increases, the heat does not dissipate sufficiently fast, and the temperature increase affects the refractive index to the extent that the laser wavelength shifts significantly. With the increase in membrane temperature, the emitted power also drops. This reflects the decrease of quantum dot gain and the increase of non-radiative recombination rates with temperature [23–25], negatively affecting both the threshold gain and the quantum efficiency.

Similar measurements were performed for InP-based PhC lasers and the thermal properties of the two platforms are compared in Fig. 4. In these plots, the peak power of the pump pulse fixed is fixed at 20 mW, which is well above lasing threshold for both samples when the duty cycle is at the smallest value of 0.1%. The peak intensity and wavelength of the emitted pulses are plotted as a function of the duty cycle (or the averaged pump power, as shown by the top axes) for both material platforms. Compared to the InGaAsP sample, the emitted power and the wavelength of the InP sample are nearly unaffected by the value of the duty cycle (in the investigated range), clearly showing the superior thermal properties of the InP material platform.

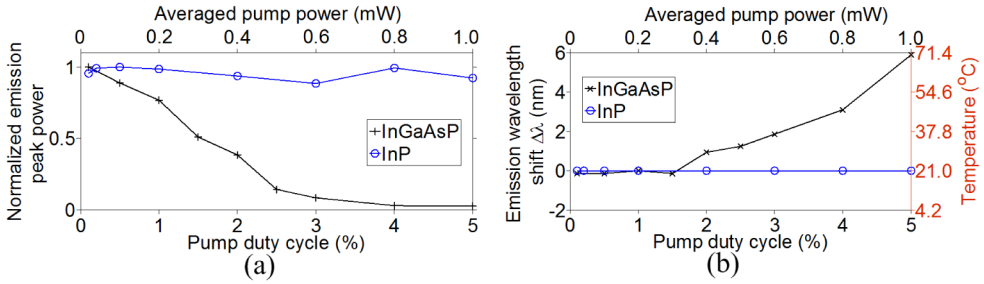

Fig. 4. Measured (a) peak power and (b) wavelength of the emitted pulses from InGaAsP (black cross) and InP (blue circle) PhC laser samples as a function of the duty cycle of the pump pulse train. The peak power of the pump pulses is fixed at 20 mW. The top axes show the time-averaged pump power. The curves in (a) are normalized by their values at the lowest duty cycle of 0.1%.

#240193 Received 1 May 2015; revised 22 Jun 2015; accepted 29 Jun 2015; published 6 Jul 2015

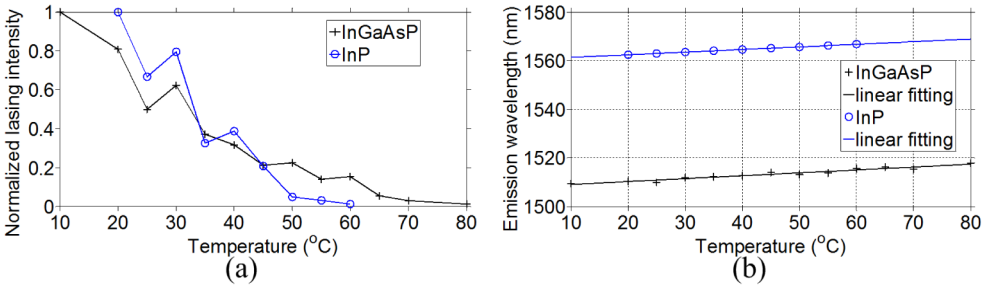

Fig. 5. Measured lasing characteristics versus sample temperature. (a) Detected power and (b) lasing wavelength for InGaAsP (black crosses) and InP (blue circles) PhC lasers.

We further quantify the thermal properties by attaching the samples to a temperature controlled stage allowing to control the temperature from $10^{o}C$ to $80^{o}C$ with an accuracy of $\pm 0.5^{o}C$. The smallest duty cycle of 0.1% is chosen in order to minimize the temperature rise induced by the optical pump. The measurements are shown in Fig. 5. The lasing wavelength linearly red-shifts with temperature, and from a linear fit we deduce a slope of $0.119nm/^{o}C$ for InGaAsP and $0.108nm/^{o}C$ for InP. Using these values, the absolute temperatures in Fig. 4(b) can be deduced and are shown by the right axis. As the duty cycle increases from 0.1% to 5%, the InGaAsP sample heats up to a value of $70^{o}C$, while the InP sample remains at room temperature, around $21^{o}C$. It should be emphasized that the temperature values stated correspond to the steady state situation. Furthermore, we neglect the spatial variation of the temperature, which will be addressed by full 3D simulations in the next section.

The superior thermal properties of InP-based PhC lasers can be attributed to two aspects. Firstmost, InP has a thermal conductivity ($68\mathrm{Wm}^{-1}K^{-1}$), which is an order of magnitude higher than InGaAsP ($6.8\mathrm{Wm}^{-1}K^{-1}$) [18]. Secondly, the photon energy (1.266 eV) of the 980 nm pump beam is larger than the bandgap (1.13 eV) of InGaAsP ($In_{0.77}Ga_{0.23}As_{0.503}P_{0.497}$), but smaller than InP (1.34 eV) at room temperature. In the InP sample, the pump beam is only absorbed in the QDs themselves and the wetting layers, whereas the InGaAsP membrane itself absorbs part of the pump energy. To minimize the effects induced by the different absorption efficiencies at 980 nm, a CW 1480 nm laser beam is next used as the excitation source. At this wavelength, the pump photons are absorbed in the quantum dots themselves for both material platforms.

#240193 Received 1 May 2015; revised 22 Jun 2015; accepted 29 Jun 2015; published 6 Jul 2015

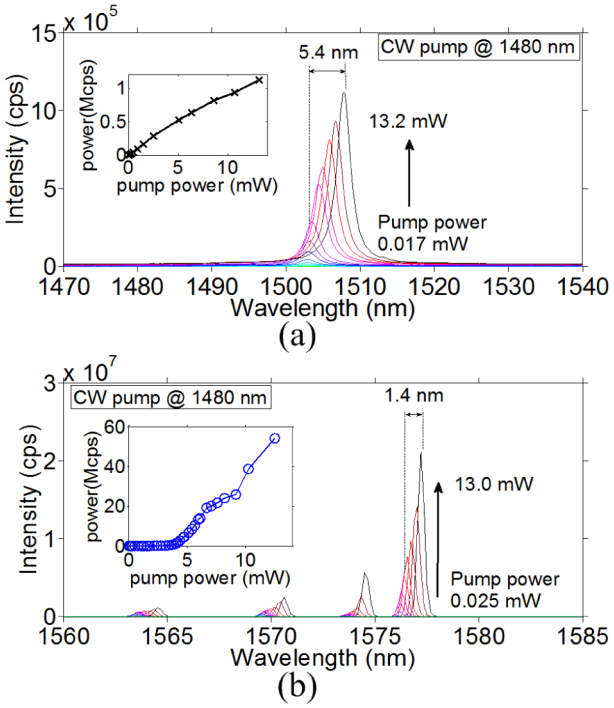

Fig. 6. Measured emission spectra for a CW 1480 nm pump beam. (a) InGaAsP PhC laser and (b) InP PhC laser. The different colors in the main plots are for different pump power levels. The insets show the intensity of the dominating peak as a function of the pump power.

For the InGaAsP sample, Fig. 6(a), a broad emission spectrum and the linear increase of emitted power with pump power indicate below-threshold operation. CW pump power levels higher than 14 mW were observed to generate so much heat that the membrane burns. The large (5.4 nm) red-shift of the wavelength observed when increasing the pump power from 0.017 mW to 13.2 mW can be attributed mostly to thermal effects. Compared to the red-shift induced by pumping at 980 nm over the same pump power range, heating is significantly less, but still prevents the observation of CW lasing in InGaAsP PhC lasers.

Emission spectra from an InP PhC laser for various pump levels are depicted in Fig. 6(b). In this case lasing is clearly observed and thermal effects only induce a red-shift of 1.4 nm, much smaller than for InGaAsP. Several cavity modes are observed. For the longest-wavelength mode, often denoted the fundamental mode, the light-out-light-in measurement in the inset of Fig. 6(b) gives a lasing threshold of ~4 mW.

4. Simulations

The temperature changes derived above are based on the assumption that the temperature is uniform over the PhC laser structure. Here, we examine this by simulating the spatial profile under the given pump conditions and membrane geometry. The thermal characteristics of an optically-pumped PhC laser depend on several factors [26]. This includes the amount and location of heat that is generated, the thermal conductivity and dissipation of the structures surrounding the sources, and the operating temperature of the laser active area. We have applied three-dimensional finite element thermal simulations to predict the temperature rise. The major source of heating is hot carrier cooling and the non-radiative recombination process of the carriers generated by absorption of the optical pump [23]. The thermal dissipation of the PhC laser region is assumed to take place mainly via conduction through

#240193 Received 1 May 2015; revised 22 Jun 2015; accepted 29 Jun 2015; published 6 Jul 2015

the surrounding bulk materials. For simplicity, we neglect the heat source variation along the membrane thickness and define the heating power density $P_{heat}(W/m^3)$ in the membrane as:

$$P_{heat}(x,y,z) = \eta \cdot P_{pump}(x,y) \cdot (1-R) \cdot \frac{1-\exp(-\alpha dL)}{dL}$$

Here P_{pump} is the optical pump power, $R = 0.3$ is the optical power reflectivity when pumping from the top along the normal of the membrane, $\alpha = 10^4 cm^{-1}$ is the absorption coefficient for the InGaAsP membrane at the 980nm pump wavelength and $dL = 340nm$ is the active material thickness (equal to the membrane thickness). Thus, approximately 20% of the total pump power, P_{pump}, is absorbed in the membrane. Furthermore, η is the fraction of the absorbed pump power that leads to heating. It has several contributions, including the energy difference between the pump and emitted photons, the rate of non-radiative recombination, reabsorption of radiation and radiation transfer [27].

For simplicity, in this paper we use $\eta = 0.5$, which can vary depending on the detailed laser structure and the pumping scheme. However, the value of η will not affect the conclusions reported here.

The size of the simulated heat sink geometry is truncated to a size of $x \times y \times z : 60\mu m \times 40\eta m \times 20\mu m$ and artificial heat transfer boundary conditions [26] are applied to approximate the cooling effect of a large sample bar ($x \times y \times z : 2mm \times 1cm \times 300\mu m$).

Figure 7 shows the calculated temperature profile for a CW Gaussian pump beam at 980 nm with a FWHM-diameter of 10 μm. As the heat source induced by the optical pump is highly localized in the middle of the air-suspended PhC membrane, the temperature variations are also localized as shown in Figs. 7(a) and 7(b). Due to the air-bridge structure, the thermal transfer of the structure is only effective in close proximity to the surrounding bulky part of the sample bar. For identical heating power density profiles, the temperature increase with optical pump power is found to have a slope of $17^o C/mW$ for InGaAsP and $1.7^o C/mW$ for InP, assuming the same heat power and geometry but using the different thermal conductivities of the two materials. Figure 7(d) shows qualitative agreement with the measurements plotted in Fig. 4(b).

For a given temperature-dependent refractive index change of $\delta n/\delta T = 2 \times 10^{-4} K^{-1}$, similar for InP and InGaAsP [28], the wavelength of the fundamental resonant mode increases linearly with temperature. The resulting temperature dependent coefficient for the structure considered, i.e., taking into account the mode overlap with the semiconductor material, is found to be 0.088 nm/K, in reasonable agreement with the measurements in Fig. 5(b).

#240193 Received 1 May 2015; revised 22 Jun 2015; accepted 29 Jun 2015; published 6 Jul 2015

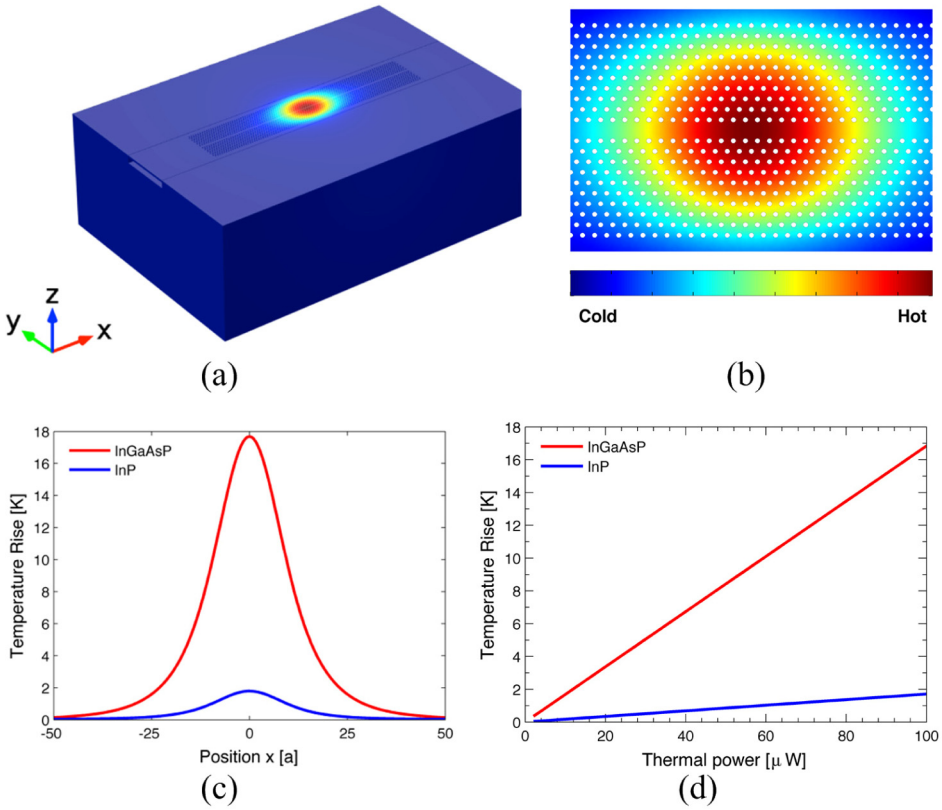

Fig. 7. 3D finite element thermal simulation of optically-pumped PhC membrane with a length of $100a$ and in room temperature environment. (a) Illustration of temperature rise induced by a fraction of absorbed CW pump power. (b) Top-view of 2D-profile of the temperature rise in the PhC membrane. (c) Calculated temperature profile in the middle of the PhC membrane waveguide for same geometry and 100 μW thermal heating power for the two material platforms. (d) Theoretical predictions of hot spot temperature rise in PhC membrane as a function of CW pump power. PhC parameters: a = 400 nm, h = 340 nm, 10 rows of air holes on each side of W1 waveguide. The color map shows the relative variation of the temperature.

5. Summary

Because of the air-embedded thin-membrane structure of PhC lasers, heating in such lasers is an important issue that may deteriorate the laser performance. In this paper we presented a systematic investigation of the thermal properties of InGaAsP and InP based PhC quantum dot lasers. We report a quantitative characterization of the induced temperature changes by examining wavelength shifts of the cavity mode. As long as the cavity mode is clearly recognized, this method doesn't require any characterization of cavity loss, even though different fabrication processes have been used for these two material platforms. As the duty cycle of the pump pulse train increases from 0.1% to 5%, InGaAsP PhC lasers can easily reach temperatures of $\sim 70^{o}C$ due to pump-induced heating, which impedes lasing. On the other hand, due to the ten-fold higher thermal conductivity of InP, PhC lasers based on this material remain at room temperature for the same range of duty cycles and lases under CW pumping. We compared the experimental results with 3D simulations of the temperature profiles of both laser structures and found good qualitative agreement.

#240193 Received 1 May 2015; revised 22 Jun 2015; accepted 29 Jun 2015; published 6 Jul 2015

Acknowledgments

We thank Sara Ek for fabricating all InGaAsP samples and Shima Kadkhodazadeh for HR STEM imaging. The authors acknowledge financial support from Villum Fonden via the NATEC Center of Excellence (Grant 8692) and the Young Investigator Programme Project QUEENs and from the Danish Council for Independent Research (FTP 0602-02623b).

#240193 Received 1 May 2015; revised 22 Jun 2015; accepted 29 Jun 2015; published 6 Jul 2015